Experimental and numerical investigation of Mg alloy sheet formability

M. Nebebe Mekonen [a], D. Steglich [a,*], J. Bohlen [b], L. Stutz [b], D. Letzig [b], J. Mosler [a,c]

[a] Helmholtz-Zentrum Geesthacht, Institute of Materials Research, Material Mechanics, D-21502 Geesthacht, Germany
[b] Helmholtz-Zentrum Geesthacht, Institute of Materials Research, Magnesium Innovations Center MagIC, D-21502 Geesthacht, Germany
[c] TU Dortmund, Institute of Mechanics, Leonhard-Euler-Str. 5, D-44227 Dortmund, Germany

ARTICLE INFO

ABSTRACT

The current paper explores experimentally and numerically obtained mechanical responses of the Nakazima-type sheet forming for the magnesium alloys ZE10 and AZ31 at elevated temperature (200 °C). The results from the experiments revealed sufficient ductility allowing sheet forming processes at the prescribed test temperature. The material's anisotropy recorded in previous experiments was confirmed. Differences in the mechanical response between the two materials in terms of strain paths during the forming experiments were quantified. The corresponding numerical responses were obtained employing a suitable constitutive model taking into account the characteristic anisotropy in deformation. In addition, for predicting limit conditions of the forming process, the localization criterion by Marciniak and Kuczynski was adopted. The constitutive model together with the localization criterion was implemented in a finite element framework based on a fully implicit time integration scheme. The reasonably good agreement between the responses of the model and the respective experiments indicated the predictive capabilities of the implemented model for the considered magnesium alloys.

© 2013 Elsevier B.V. All rights reserved.

1. Introduction

The utilization of magnesium sheets for the application as components and structures describes one step to pave the way for metallic light-weight applications. Sheets are known as a fundamental base material for forming procedures and are thus required to exploit the potential of magnesium alloys used for light-weight applications. However, drawbacks for using magnesium sheets are multifold, dealing with the need to perform forming operations at elevated temperatures, the anisotropy of mechanical properties or the limited ductility of formed parts. For the assessment of magnesium sheets and their performance, typically results of uniaxial mechanical tests, such as strength properties, ductility, normal anisotropy (*r*-value) and strain hardening behavior are used. However, forming involves many procedures with a variety of strain paths, e.g. stretch forming or deep drawing to name two of them with distinctly different contribution of material flow from the sheets' thickness or in the sheet plane. Thus, tensile testing does not suffice for evaluating forming operations.

A comprehensive way to assess the formability of sheets accounting for these different aspects is based on experiments prescribing different strain paths and limiting major strains

determined in dependence of the minor strains [26,31,15–17,13]. A (usually hemispherical) punch is applied on a work-piece until strain localization or fracture is observed in the sheet. During this process, the work-piece is clamped in place by dies. The results of such formability tests are commonly represented by the forming limit diagram (FLD), as proposed by [25]. From these tests a forming limit curve (FLC) results which represents strains of limiting uniform deformation as a function of the (linear) strain path. Limit strains are the boundary between safe and failed zones, where the region above the forming-limit strain curve is the failure zone. This measure of formability can then be applied in the design of forming procedures.

Alternatively, there is a need for accurate predictive simulation techniques for metal forming based on finite element (FE) analyses, which represent the current state-of-the-art in virtual prototyping, cf. [1]. For realistic finite element predictions, it is vital to use accurate plasticity and localization models. As the quality of the prediction strongly depends on the constitutive model used, its selection and its calibration become a key issue. Over the years, several authors have proposed a number of such models describing the yielding behavior in terms of macroscopic yield functions for various alloys, e.g. [18,20,3,24,7]. Cazacu and Barlat introduced a yield function (CaBa2004) as a modification of the Drucker model [11], accounting for the material anisotropy as well as for the stress-differential effect observed in textured magnesium alloys [8]. This plasticity model has been successfully

* Corresponding author. Tel.: +49 4152872543; fax: +49 41528742543.
  E-mail address: dirk.steglich@hzg.de (D. Steglich).

applied to predict the deformation of magnesium alloys [30] and is therefore employed in the following.

The application of the aforementioned model requires in addition a criterion for the determination of limiting conditions. Several theoretical approaches are proposed: Methods which evaluate the initiation of a localized strain band based on the plastic instability in a homogeneous sheet, cf. [36,19], and methods which establish localization from a plastic instability of a heterogeneous sheet, with the assumption of a preexisting inhomogeneity in the sheet, cf. [28,29,21]. Damage models are also proposed to predict the forming limits [10,9], but their use is numerically costly due to additional internal variables to be included in the modeling and thus they are rarely used in practice. For a comprehensive presentation of the numerical methods the reader is referred to [6,1,27]. In this work, a nonlinear approach proposed in the work of Marciniak and Kuczynski [28] (M–K model) is employed. These authors showed that the presence of an imperfection in the sheet can lead to unstable deformation in the weaker region and to subsequent localized necking and failure. Although the M–K model is one of the early imperfection theories, its concept can still be regarded as useful due to its flexibility and simplicity. Recent contributions considering the M–K model deal, e.g. with texture and slip system hardening effects on the FLD [32], strain paths changes and different combinations of yield criteria and hardening rules [2] and comparison between the M–K model and an alternative localization criterion [5].

In an attempt to determine the formability of the two magnesium sheet alloys ZE10 and AZ31 at elevated temperature, formability tests were conducted. The respective results are reported in Section 4. Numerical predictions are presented in Section 4.2 and compared with the test results in terms of both, macroscopic quantities and local strain paths. The application of an advanced plasticity model in conjunction with a localization criterion allowed a deeper insight into the interaction of field quantities and the impact of model parameter calibration, which is discussed in Section 5.

2. Materials and methods

2.1. Material under investigation

Formability tests reported in the following were conducted for two different magnesium alloy sheets (sheet thickness 1.3 mm), namely ZE10 (Mg–1Zn–Ce based mischmetal) and AZ31 (Mg–3Al–1Zn–Mn) in a heat treated condition (O-temper). The choice of these alloys is motivated by the differences in their mechanical behavior and formability, described in earlier works, see [4,34,37]. ZE10 shows improved ductility at room temperature compared to AZ31 which is associated with an effect of the included rare earth elements to weaken the crystallographic texture, resulting in higher work hardening and increased ductility.

Table 1
Mechanical responses obtained from tensile tests: yield stress (YS), ultimate tensile stresses (UTS) together with uniform (Us) and failure (Ts) strains measured for ZE10 and AZ31 at 200 °C and nominal strain rate of 0.02 s^{-1}.

Mat.	Ori.	YS (MPa)	UTS (MPa)	Us (%)	Ts (%)
ZE10	RD	86	112	17.1	50.7
	45°	78	104	19.5	73.7
	TD	80	105	19.3	64.4
AZ31	RD	80	119	12.1	53.8
	45°	81	118	10.9	53.7
	TD	86	122	10.3	52.5

The mechanical characterization of these materials under uniaxial tensile loading conditions has been detailed previously, cf. [30]. A summary of the resulting responses is exemplarily presented in Table 1 in terms of the in-plane yielding behavior and ductility and in Fig. 1 in terms of r-values, the normal anisotropy, as a function of accumulated plastic strain. The differences in the yield stresses between the different specimen orientation and r-values reveal the materials anisotropy. Contrary to the common assumption, the computed r-values also show a strain dependence, which is pronounced in case of AZ31. A positive strain rate effect on the yield strength is recorded while the opposite effect was observed on the ductility. Moreover, the strain rate influence on the material's anisotropy is small. The reasonably large level of
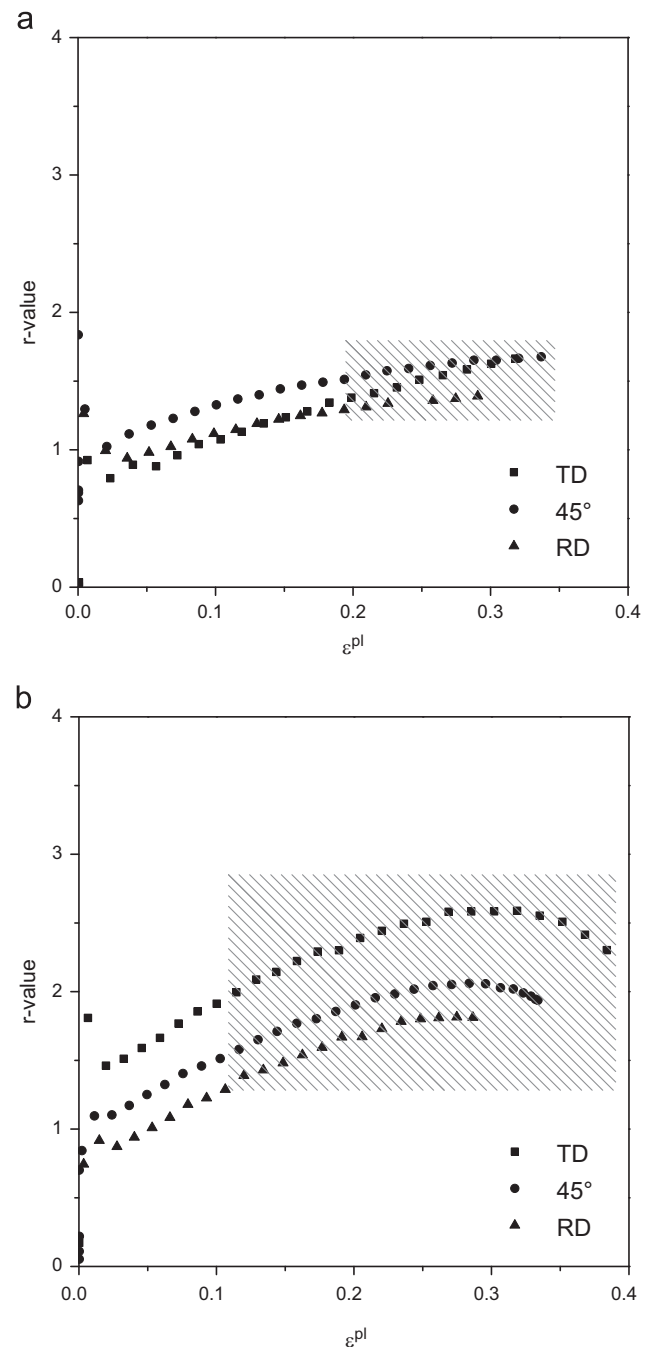
Fig. 1. r-Values measured for ZE10 (a) and AZ31 (b) at 200 °C at a strain rate of 0.02 s^{-1} [30]; the shaded section indicates localized deformation.
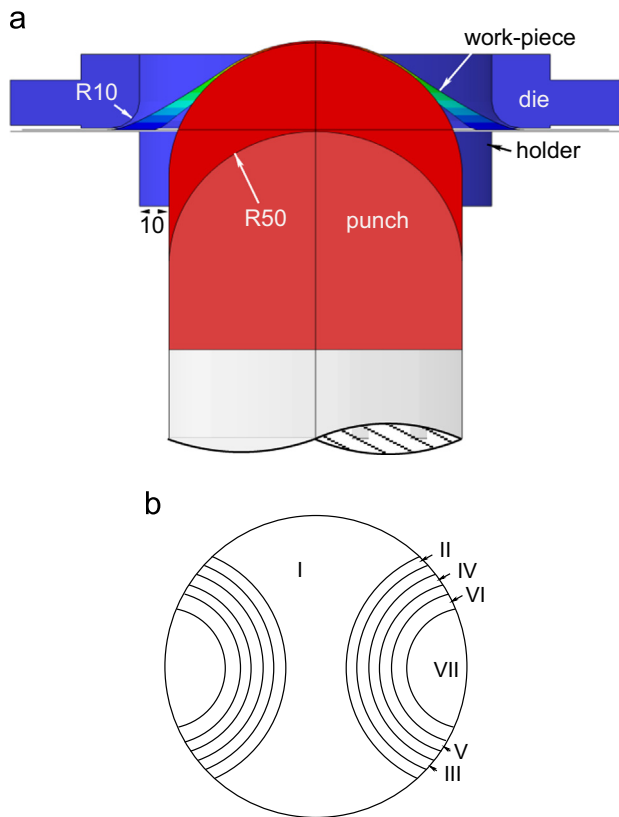
Fig. 2. Forming limit test setup (a) and work-piece geometries proposed by Hasek [14] (b). Measures in millimeters.

Fig. 3. Principle for the determination of forming limit strains based on synchronization of force and the strain responses.

deformation for both alloys implies the suitability of the test temperature for a sheet forming process.

2.2. Nakazima-type sheet forming test

The Nakazima-type forming limit tests were conducted based on the ISO 12004 standard using a universal sheet metal testing machine (ERICHSEN® 145-60). The dimensions of the tool geometry are given in Fig. 2a. The tests constitute seven circular work-pieces with an outer diameter of 200 mm and recesses of different radii, namely 0, 40, 50, 57.5, 65, 72.5 and 80 mm [14], see Fig. 2b. It is worth to mention that the recesses on the work-pieces are all made perpendicular to the rolling direction. The tests cover the negative as well as the positive domain of the FLD, i.e. negative and positive minor principal strains. In addition, the strain responses obtained from the different geometries during the forming tests should follow linear paths in the FLD, cf. [1]. The test temperature was maintained at 200 °C. This was established by heating up the tools, i.e. the die, holder and punch, along with the work-piece in a separate furnace prior to forming. As recommended by the ISO standard, the punch speed was set to 1 mm/s. The clamping force applied to hold the work-piece in place without causing edge fracture was set to 300 kN. The lubrication between the punch and the work-piece was established by the use of PTFE foil placed between two layers of lubrication oil. For checking the reproducibility of the test results, at least two work-pieces per geometry were tested. In addition to the force response and punch displacement, the history of the deformation field was recorded using a digital camera connected to an optical strain measuring system (ARAMIS®). The use of this optical system requires special surface treatment of the test specimens, necessary for establishing a stochastic pattern that can be analyzed with image processing tools. The samples for Nakajima test were
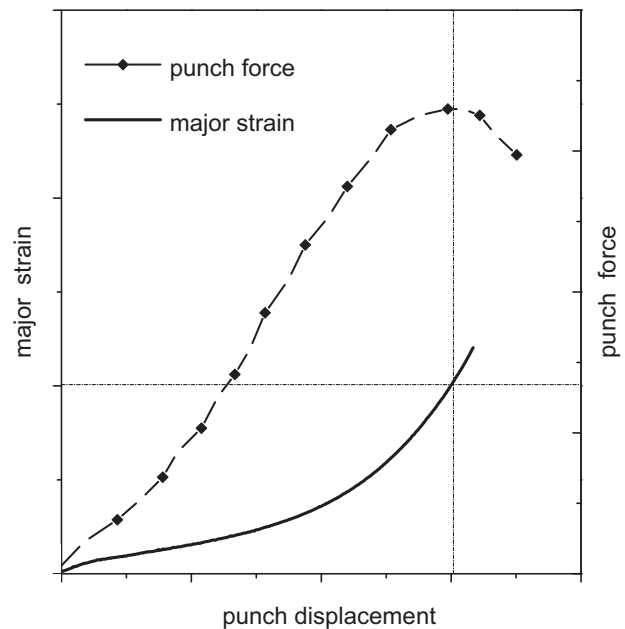
cleaned with ethanol and sprayed with a white layer of a developer medium (Medium Nr. 3 – Entwickler of Fa. Helling GmbH) which has shown to be resistant against heating in the temperature range of this study. A stochastic black pattern for measuring with ARAMIS® was then carefully sprayed with a graphite spray (Graphit 33 of Kontakt Chemie).

2.3. Methods for establishing the forming limits

For establishing the forming limits a method was elaborated which makes use of the force–punch displacement signal of the forming test and the strain response recorded from the sheet. The force–displacement and strain–displacement signals were synchronized. The maximum of the force–displacement curve was assumed to indicate the onset of strain localization in the sheet, referred to as softening point, see Fig. 3. Thus, the limiting strain components can be derived from the recorded strain field corresponding to the maximum punch force.

This method avoids fitting or usage of approximation functions over the ISO 12004 standard. In addition to the forming limit curve, a failure curve was established through a visual inspection of the deformation history. This failure curve indicates the strain levels at the onset of failure defined by the initiation of macro cracks. Taking advantage of the continuous deformation field measurement from the ARAMIS® system, it was possible to obtain strain paths for each work-piece employed in the forming limit tests. These strain paths were established by computing the major and minor in-plane principal strain for selected points in the neighborhood of a crack located at the center of the work-pieces.

2.4. Finite element model

The finite element (FE) modeling of the forming process aimed at matching the numerically obtained strain history to the one extracted from the experiments. Thus, the FE model followed directly from the experimental setup. The model was composed of three rigid tools (die, holder and punch) together with the work-piece, see Fig. 2a. According to Fig. 2b, the work-piece adopted seven different geometries covering strain states of the complete forming limit diagram. The tools and the work-pieces were assembled

in a 3D modeling space. The work-piece was discretized with 4-noded linear shell elements with reduced integration. Numerical studies focusing on the punch force response and the strain localization pattern of the work-piece considering a 3D discretization revealed that the modeling error while using shell elements is small. In order to further reduce the computational cost, an orthogonal symmetry was assumed. In practice, the tools undergo negligible deformation and are therefore represented by rigid bodies. Isothermal conditions were assumed within the simulations.

The interaction between the tools and the work-piece is an important aspect in the forming process. The simulations performed in this work adopted the so-called hard contact. This method ensures the most accurate prediction of the contact while challenging the convergence behavior of the simulation. Instead of prescribing displacement boundary conditions to the work-piece, a normal force of 300 kN was exerted by the flat region of the die onto the work-piece representing the holder force. The tangential constraint was applied by introducing a Coulomb-type friction. The interaction between the punch and the work-piece was also governed by friction and a pressure exerted by the motion of the punch. The amount of friction used in the simulations was assessed by monitoring the punch force record and the point of strain localization in comparison with the experiments. While an increase of the friction coefficient leads to a generally higher punch force for all geometries, the point of strain localization moves away from the pole of the tool. As a matter of fact, the amount of friction is very small as a consequence of the lubrication described earlier. From these observations, the friction coefficient was found to be close to zero ($\mu \approx 0$) for this interaction pair. All simulations reported in the following were conducted using the implicit solver of the commercial code ABAQUS®. The underlying constitutive model, which will be briefly described next, was implemented as a user-defined subroutine (UMAT).

3. Constitutive model and localization criterion

3.1. Plastic deformation

A yield function suitable for describing the plastic deformation of magnesium alloys should capture the stress differential effect and the anisotropy of the material. A function based on tensor transforms complying with such requirements was presented in a series of papers by Cazacu and co-workers, cf. [8]. This function was also adopted in the present paper. The model was re-formulated in terms of Mandel stresses automatically fulfilling the principle of material frame indifference. Furthermore, it was rewritten in tensor notation. Functions were introduced for the model coefficients [12,33], allowing to account for distortional hardening (distortion of the yield function). The numerical procedure considered in this work adopts a constitutive model presented in [30]. For the sake of clearness the formulation is given in the Appendix.

The feature of the model to predict a variation of the strain ratio with increasing deformation directly evidences the distortional character of the calculated deformation. The change of the direction of the plastic strain increment requires a change in the yield surface shape. This is modulated by a term referring to the shape change. Strain hardening in the current model consists of two parts: The distortional part expressed by transformation tensors $\mathbb{H}_i$ depending on the accumulated plastic strain α (see Eqs. (A.17) and A.6)) and an isotropic part depending on the accumulated plastic stain α and the current strain rate $\dot{\alpha}$ (see Eqs. (A.16) and A.9)). The isotropic part naturally does not depend on the loading direction. In contrast, the distortional part allows

Table 2
Anisotropy parameters of the plasticity model.

	$\mathbb{H}_1$			$\mathbb{H}_2$		
	A	B	C	A	B	C
ZE10						
c_1	−4.5	2.7	0	1.0	−5.9	6.5
c_2	−4.1	−6.5	0.1	1.2	−2.2	3.2
c_3	−3.5	−3.1	8.8	5.8	0.0	3.1
c_4	4.1	1.9	10.4	−5.4	3.4	3.9
c_5	1	0	0	0	0	0
c_6	1	0	0	0	0	0
AZ31						
c_1	1.7	−1.9	0.3	2.1	−0.8	4.4
c_2	1.6	2.5	0.0	−1.5	0.6	0.8
c_3	−3.2	−2.4	3.1	0.5	2.5	1.0
c_4	1.6	1.7	2.8	−0.9	−1.2	3.3
c_5	1	0	0	0	0	0
c_6	1	0	0	0	0	0

Table 3
Hardening parameters of the plasticity model.

Mat.	$\Delta\tau_\infty$ (MPa)	ζ ()	τ_0 (MPa)	β (1/s)	$n()$
ZE10	59.212	−8.752	87.385	2.384E−2	0.0454
AZ31	42.069	−21.147	52.140	2.185E−4	0.0841

for a strain-dependent change of the yield surface's shape. A dependency on the strain rate in this part is not included, as experimental results indicate that material anisotropy is not significantly affected by the strain rate. Details on the determination of the model parameters are given in [30]. Tables 2 and 3 summarize the model parameters for both materials under investigation, ZE10 and AZ31.

3.2. Marciniak and Kuczynski localization criterion

For predicting limit strains of sheet forming processes, Marciniak and Kuczynski introduced a localization criterion, the so-called M–K-criterion, cf. [28]. This method assumes the existence of an infinite long band of inhomogeneity in an otherwise homogeneous work-piece. In the original work, the inhomogeneity band is oriented along the minor principal deformation direction of the work-piece. Localization is assumed to occur once the ratio of the strains in the inhomogeneous to that in the homogeneous region exceeds a prescribed critical value. The resulting limit strains are presented in the so-called Forming Limit Diagram (FLD), cf. [25]. The original M–K approach span only the positive domain of the FLD, that is, only positive minor principal strains were considered. This model was later improved by assuming an arbitrary orientation of the inhomogeneity, see [21–23]. Such improvement allowed the prediction of the limit strains for both the negative and the positive domains of the FLD.

In this work, a further improved version of the M–K-criterion is elaborated and subsequently applied. In contrast to most of the previous models, no explicit assumption concerning the strain field within the homogeneous and the inhomogeneous region is made, i.e. fully three-dimensional deformation states are consistently covered and three-dimensional constitutive models can be directly employed. Plane stress conditions characterizing the stress state within sheets are iteratively enforced.

Like the original M–K-approach, the inhomogeneity band is introduced in terms of a reduced thickness t^b of the work-piece. The orientation of the band with respect to the reference configuration is
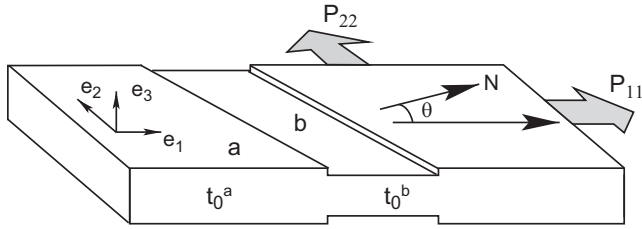
Fig. 4. Schematic representation of M–K model, cf. [28,22,23].

represented by the normal vector N, see Fig. 4. Without loss of generality, a time-invariant cartesian coordinate system (e_1, e_2, e_3) whose orthogonal base vectors e_1 and e_2 span the domain of the undeformed sheet (reference configuration) is chosen. Consequently, N belongs to the e_1–e_2–plane and is uniquely defined by the angle θ in Fig. 4. For the sake of simplicity, quantities characterizing the band of inhomogeneity are represented in the following by the superscript $()^b$, while those characterizing the homogeneous region are represented by the superscript $()^a$. Accordingly, the deformation gradient in the band is denoted as F^b and that corresponding to the homogeneous region is denoted as F^a.

In line with the standard MK-approach, localization is assumed to occur, once the thickness of the band relative to that of the surrounding region reaches a certain critical minimum value. Within the most general fully three-dimensional setting, the relative thickness can be written as

$$\gamma := \frac{t^b}{t^a} = \frac{\| F^b \cdot e_3 \|}{\| F^a \cdot e_3 \|} \frac{t_0^b}{t_0^a} \tag{1}$$

where t_0^a and t_0^b are the initial thicknesses, while t^a and t^b are those belonging the deformed configuration. A spatially constant deformation gradient (strain) within both regions has been assumed in Eq. (1).

The relation between the homogeneous and the inhomogeneous regions is established in the M–K-approach through conditions of geometrical compatibility and equilibrium. Concerning the latter, equilibrium at the interface under the assumption of constant stresses in thickness direction in both domains requires

$$t_0^a [P^a \cdot N] = t_0^b [P^b \cdot N]. \tag{2}$$

Here, P is the first Piola–Kirchhoff stress tensor (engineering stresses). Clearly, Eq. (2) can be equivalently written in terms of Cauchy stresses (true stresses). While the equilibrium condition (2) is standard, the classical compatibility condition is too restrictive for the M–Kapproach. This will be explained next.

The classical Hadamard compatibility condition at the interface reads

$$[[F]] := F^b - F^a = a \otimes N. \tag{3}$$

In this equation, $a \in \mathbb{R}^3$ is an arbitrary vector. Thus, only three effective components of the deformation gradients in the band and the homogeneous region are different. Considering a uniaxial stress state in e_1–direction for a fully isotropic constitutive model (the deformation gradient shows then a diagonal structure), Eq. (3) implies $F_{33}^a = F_{33}^b$. As a result Eq. (1) leads to $\gamma = t_0^b / t_0^a = \text{const}$ and localization cannot occur. Hence, the modified compatibility condition

$$[[F]] := F^b - F^a = a \otimes N + \Delta F_{33} e_3 \otimes e_3 \tag{4}$$

is considered. The other components of the deformation gradient associated with the thickness direction, F_{13}, F_{23}, F_{31} and F_{32}, do not need to be taken into account. Due to the orthogonal material

symmetry resulting from the rolling process and due to plane stress conditions, they automatically vanish, cf. [27].

By inserting the relaxed compatibility condition (4) into the equilibrium condition (2), the residual

$$R(a, \Delta F_{33}) := t_0^a [P^a \cdot N] - t_0^b [P^b \cdot N] \tag{5}$$

can be introduced. It is obvious that $R = 0$ cannot be solved uniquely, since it is a set of three nonlinear equations depending on four unknowns. The missing additional condition is that enforcing a plane stress state also in the band, i.e.
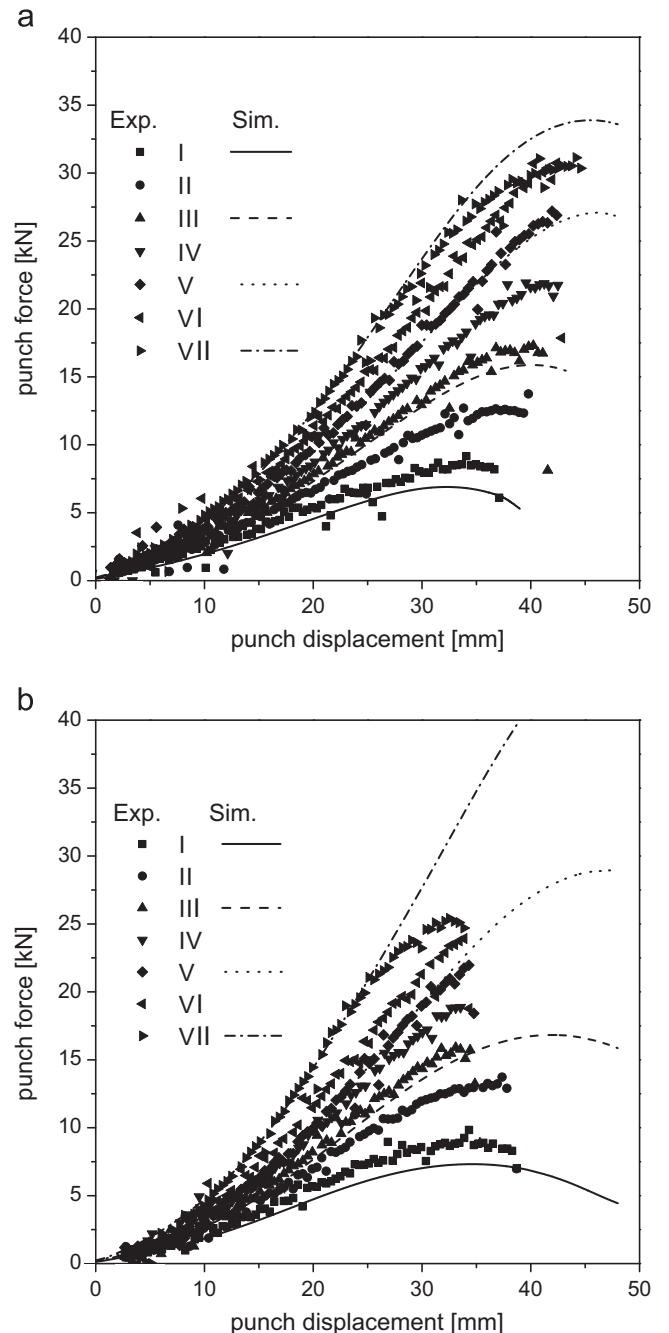
$$P_{33}^b = 0. \tag{6}$$

Fig. 5. Punch force–displacement responses observed in experiments (symbols) and of the forming limit simulations (lines): ZE10 (a) and AZ31 (b).

Finally, it is important to note that the system of Eqs. (5) and (6) depends also on the orientation of the initial imperfection, i.e. on $N = N(\theta)$. The most critical orientation is that leading to the strongest thickness reduction of the band. As a consequence, the algorithm linked to ABAQUS® via the user subroutine UMAT reads

$$\text{minimize}: \quad \gamma(\theta) = \frac{t^b}{t^a} \qquad (7)$$

$$\text{subject to}: \quad \mathbf{R} = \mathbf{0} \text{ and } P_{33}^b = 0. \qquad (8)$$

Within the implementation, the minimization (7) is done by varying the angle θ starting from 0° in steps of 1°. Localization is considered to occur when

$$\gamma > \gamma_{\text{crit}}. \qquad (9)$$

Here, $\gamma_{\text{crit}} = 10$ is employed, cf. [1]. However, the choice of this value is rather arbitrary, cf. [22,27].

4. Nakazima-type forming test results

4.1. Experimental results at 200 °C

The mechanical responses obtained from the forming limit tests are presented here in terms of punch force–displacement curves, strain paths, as well as limit and failure strain curves. The punch force–displacement curves in Fig. 5 demonstrate the effects of the work-piece geometries on the force response and the extent of formability. Experimental results are indicated by symbols. The general observation for both ZE10 and AZ31 is that a decrease in radius of the recess increases the punch force response. This is a direct result of the larger cross-section and an increased constraint associated with a sharpening of the work-pieces recesses from geometries I to VII, see Fig. 2b. Furthermore, the larger punch displacement achieved in the case of ZE10 compared to that of AZ31 associated with a higher load level indicates its improved formability. Note that up to a punch displacement of 25 mm AZ31 revealed a slightly higher load level than ZE10. The further increase in force in the case of ZE10 can be attributed to its improved ductility and associated hardening characteristics evidenced during tensile testing [30].

Strain paths obtained from the optical system are shown in Fig. 6. In order to avoid overloaded graphs, only those strain paths resulting from geometries I, III, V and VII are considered in the following. The strain history at the pole of each specimen basically follows linear paths. The small deviation at the early stage of forming results from stretching of the sheet over the hemispherical punch. Thus, the limit strains at the center of the work-pieces can be approximated by offsetting the measured limit strains on the surface of the work-pieces by the positive strains. Differences in the principal strain paths between the two materials were also observed during the forming of the fully circular work-piece (geometry VII), for which an equi-biaxial loading condition is generally assumed. While for geometry VII the strain path appears as a straight line in case of ZE10, the major strain is evolving more rapidly than the minor strain in case of AZ31. It is even more significant that the work-piece with the largest recess, designed to be close to an uniaxial loading state, resulted in a strain ratio different from the theoretical value of -2. This observation reaffirmed the anisotropic behavior of the materials considered.

Driven by the relatively early localization observed during the uniaxial tensile test, the reference limit strain data were here taken from the equivalent forming test responses, specifically from geometry I. Hence, the FLC in Fig. 7 indicates a level of limit strain as high as 0.5 in the uniaxial-like state (geometry I), but approximately 0.3 for AZ31 and 0.4 for ZE10 limit strain in the equi-biaxial
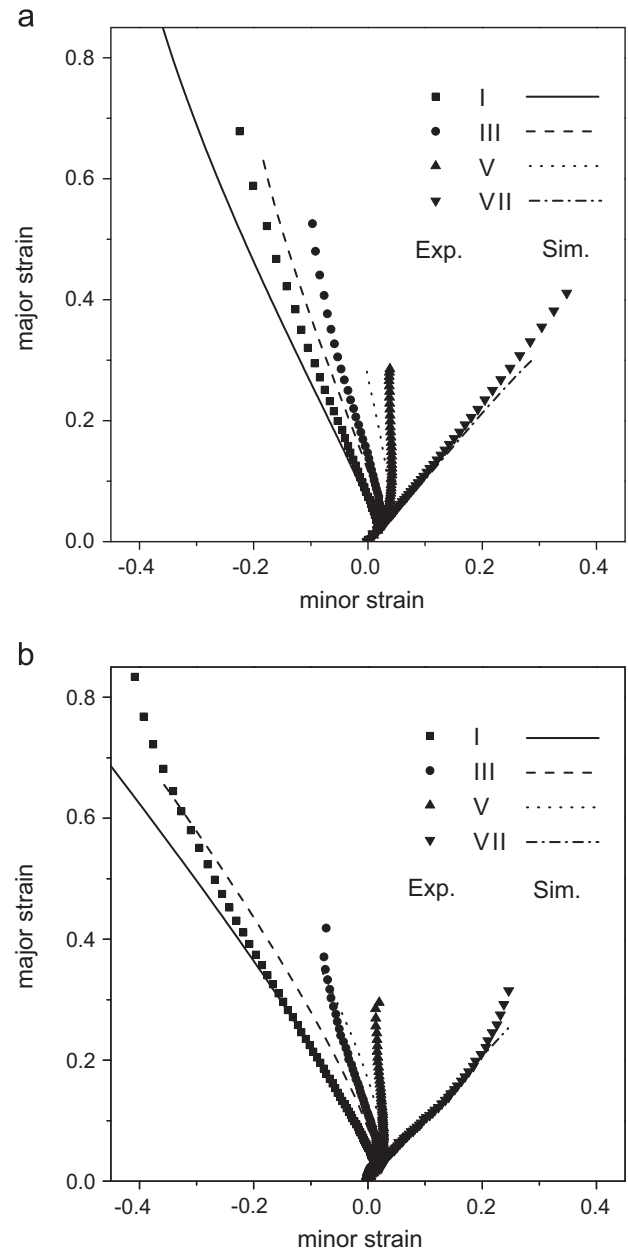

Fig. 6. Comparison of selected experimentally measured (symbols) and numerically predicted (lines) strain paths for ZE10 (a) and AZ31 (b).

state (geometry VII) of deformation. This reveals a level of deformation generally sufficient for a practical forming application. Moreover it is observed that the difference between the failure strain and the forming limit strain is larger in the negative domain of the FLD than in the positive domain. This is consistent with the large amount of nonuniform deformation reported during the uniaxial tensile test presented in [30]. However, the strain at localization of the forming test (approximately 0.5) and the strain at the start of the diffuse necking of the uniaxial tensile test, approximately 0.2 (in the case of ZE10) and 0.13 (in the case of AZ31), differ from each other significantly.

4.2. Simulations

4.2.1. Punch force–displacement and strain paths

The forming process was reproduced by means of a finite element simulation described in Section 2.4 using the calibrated
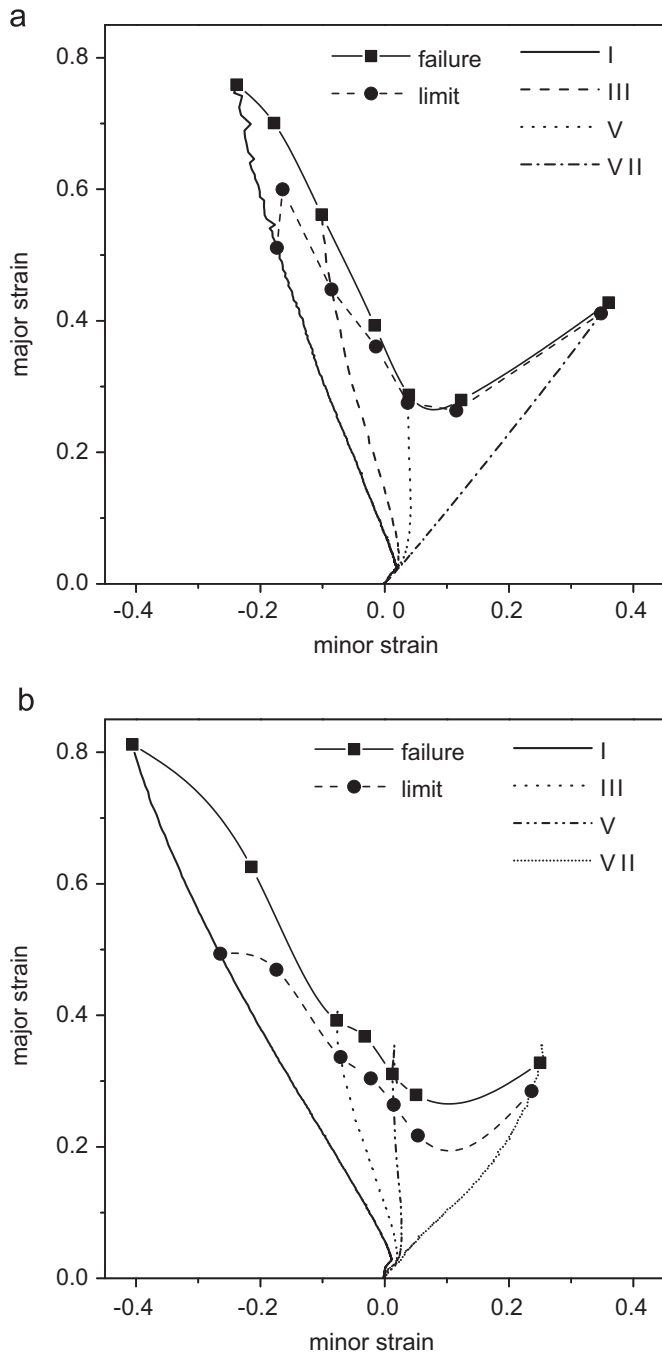
Fig. 7. Measured forming limits and failure curves: ZE10 (a) and AZ31 (b).

improvement of the responses could possibly be achieved by a more careful assessment of the *r*-value evolution at a high level of deformation. This will be considered hereinafter.

Together with the in-plane principal strains measured at the middle of the upper surface of the work-piece, the corresponding computed strain paths are analyzed. As it is shown in Fig. 6, all work-piece geometries resulted in linear strain paths for higher deformation levels. Consistent with the experimental response, an offset in the minor principal strain into the positive domain of the forming limit diagram is also observed. This is particularly pronounced for geometries which exhibit negative minor strain values, such as geometries I and III. Such effects can be explained by the stretching of the work-piece. According to Fig. 6, the strain paths are captured better for geometries I and VII of AZ31 than for geometries III and V. The significant difference in the strain paths between experiments and simulations for geometries III and V for AZ31 is evident.
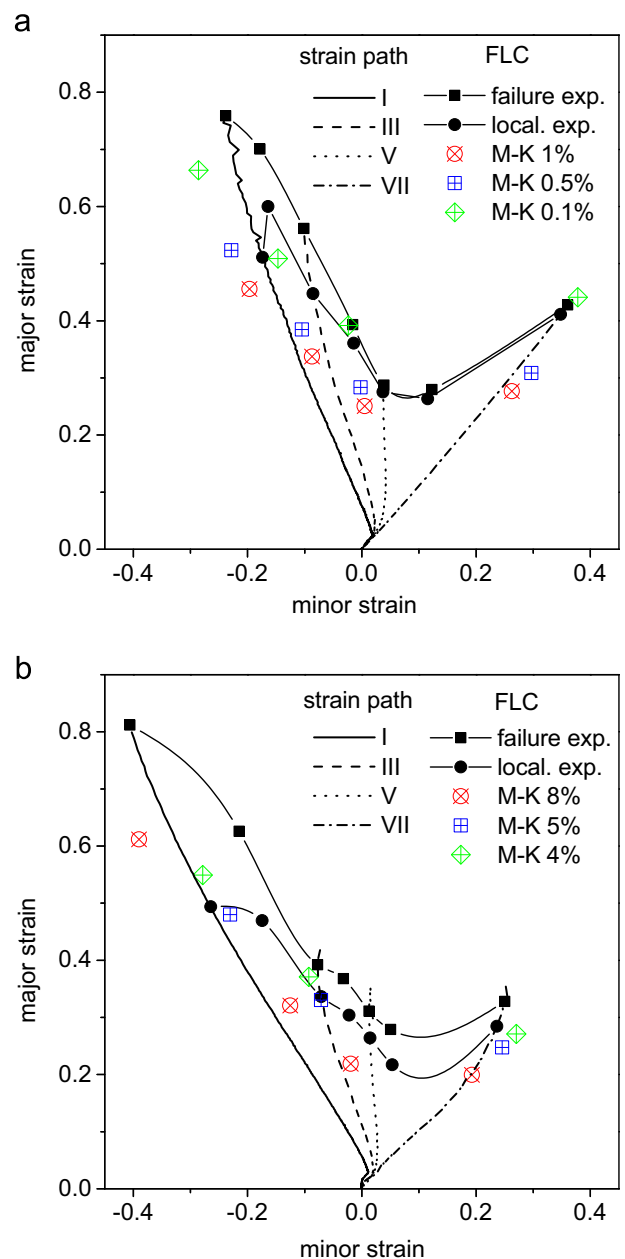
Fig. 8. Comparison of experimentally measured and numerically predicted limit strains for ZE10 (a) and AZ31 (b).

constitutive model outlined in Section 3. The numerically predicted force responses for the configurations I, III, V and VII are included in Fig. 5. For both considered materials the predicted force responses show a reasonably good agreement with the experiments. However, the forces for higher deformation levels are either underestimated in the cases of geometries I and III, or slightly overestimated in the cases of geometries V and VII. This effect is more pronounced for AZ31 than for ZE10. While the overestimation in the case of geometries VII and V can be explained by the absence of a damage criterion in the modeling, the overestimation of the force for the low stress triaxiality geometries I and II may result from the calibration of the plastic potential. At this point, it is assumed that the *r*-values shown in Fig. 1 may have contributed to this underestimation. Thus,

4.2.2. Forming limits

Finally, the numerical prediction of the forming limit strains is presented by employing the M–K localization criterion, see Section 3.2. Such predictions require the definition of a geometrical imperfection in the homogeneous work-piece, as results strongly depend on this assumption. The magnitude of this imperfection is often calibrated based on a simple uniaxial tensile test. The required imperfection was obtained here by performing simulations with different imperfection magnitudes. The responses obtained from these simulations are presented in Fig. 8. It can be seen that the higher the initial imperfection, the earlier the localization occurs. The range of imperfection values required strongly depends on the material considered. In the case of ZE10, the required imperfection for the M–K model is about 0.1%. In the case of AZ31 with the distortional hardening model, imperfection values between 4.0% and 5.0% lead to limit strains within the range of the reference values observed in the respective experiments, see Fig. 8. These values are surprisingly high. Usually, the values for initial imperfections leading to realistic predictions of the forming behavior range are taken from the interval [0%, 1%] [32]. This fact, together with apparent mismatch of the strain path for geometries III and V, calls to reconcile the plasticity model used in the simulations of the forming behavior of AZ31. In particular, an investigation regarding the effect of r-value is presented below.

4.2.3. Re-calibration of constitutive model for AZ31 assuming constant r-values

As described above, the constitutive law allows for a description of distortional hardening of the material. The respective model parameters were calibrated based on the evolution of r-values taken from tensile tests along three independent orientations, i.e. 0°, 45° and 90° with respect to the rolling direction of the sheet, see Fig. 1. While the measurement of the plastic strain ratio is straightforward as long as the deformation is uniform, it becomes challenging once necking occurs. In the experiments reported, the r-values were continuously determined over the whole range of deformation using optical strain field measurements as a local quantity (compare the shaded region in Fig. 1). Although still a valid number, its significance is diminished in the necking regime compared to the previous (uniform) stage. In order to investigate the influence of this particular input on material characterization, simulations based on the re-calibrated constitutive model assuming constant r-values taken at strain levels of 0.03, 0.08 and 0.12 were performed for AZ31. All three values are in the range of uniform deformation. Depending on the orientation of the respective specimen during tensile testing, this leads to r-values between 0.85 and 1.45 (strain of 0.03), 1.2 and 1.8 (strain of 0.08) and 1.4 and 2.2 (strain of 0.12). Based on this input, the complete identification procedure was repeated, assuming constant parameters in the transformation tensors $\mathbb{H}_i$, compare Table 1b. The distortional character of hardening is suppressed in this approach, while the orthotropic anisotropy of the material is still considered.

The force–displacement curves for geometry I in Fig. 9a reveal that a change in the r-value has a relatively small effect on the force response. The simulation with a variable r-value results only in a slightly higher force response. In contrast to that the figure shows considerable differences in the force responses for geometry VII. In particular, the S-shape of the force–displacement curve is captured by the simulations assuming a constant r-value, but not with a variable r-value. The latter tends to delay strain localization in the sheet, while the simulations based on a constant r-value predict the experimentally obtained force response more realistically. Note that the same effect can be observed in geometry I which, however, appears to be less pronounced. A high r-value
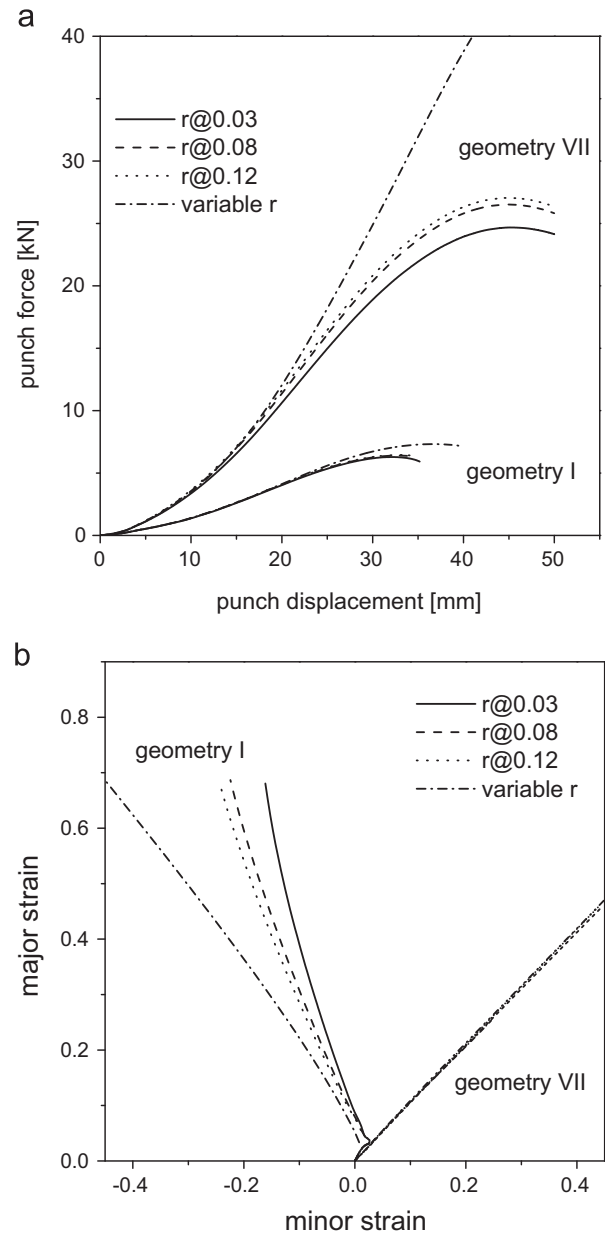

Fig. 9. Effect of the parameter identification procedure on the punch force predictions (a) and strain paths (b) for two geometries of the Nakazima test of AZ31.

indirectly influences the biaxial stress–strain curve, because the resulting yield surfaces become elongated in direction of the equi-biaxial (plane) stress state leading to an overestimation of the (biaxial) stress. Due to the fact that experimental data related to equi-biaxial stress states are not included in the calibration process of the plasticity model, the resulting yield surfaces are determined by the (uniaxial) stress signal in 0°, 45° and 90° as well as the yield surface's slope while intersecting the x- and y-axes of the plane stress representation. Consequently, the prediction of the biaxial stress strain curve becomes vague. From this it can be concluded that the extrapolation used for the determination of r-values is not optimal.

The strain path of geometry VII is hence less affected by the choice of the r-value, see Fig. 9b. As expected, geometry I reveals significantly different strain paths depending on the plasticity model: a shift to the left of the FLD domain with an increasing
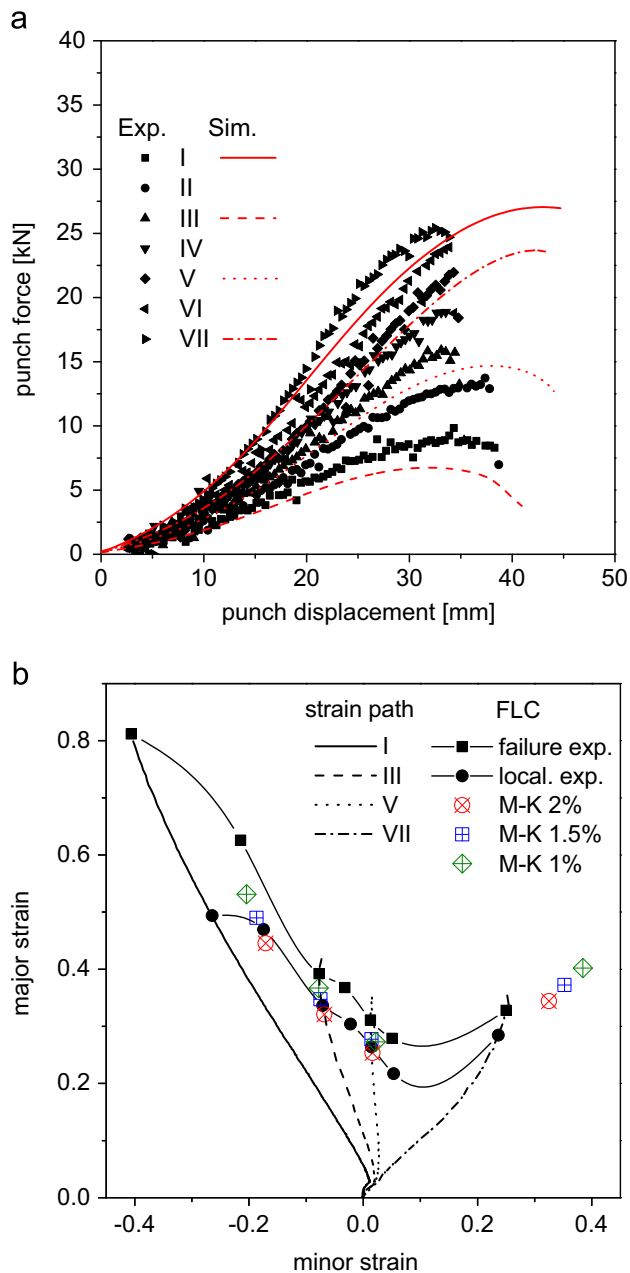
reveals the forming limit. The strain path of geometry I is still not captured to its full extent, but an improvement compared to Fig. 7b could be achieved for AZ31.

5. Discussion and conclusions

The large number of process parameters involved in sheet forming generally makes experimental investigations of the process very expensive. Therefore, numerical analyses are efficient and promising substitutes. For that purpose, a constitutive model was adopted from [30], calibrated and implemented within the finite element program ABAQUS® using an implicit integration scheme. This physically sound constitutive model was employed along with a localization criterion for the corresponding numerical analyses.

The mechanical responses of the forming experiments revealed sufficient formability at the test temperature (200 °C). This was illustrated by a 0.5 limit major strain in the uniaxial state and a 0.3 limit strain in the equi-biaxial state of deformation. Moreover, and consistent with the large amount of nonuniform deformation recorded during the uniaxial tensile test, a large difference between the failure strain and the forming limit strain was observed in the domain of negative minor strain of the FLD.

Although the uniaxial tensile tests used for the calibration of the material model and the Nakazima tests were carried out at the same temperature, significant differences in the case of geometry I in the resulting limit strains and fracture strains were recorded. Such differences require some attention because the experimental information of uniaxial testing determines the simulated mechanical response. In the case of uniaxial tensile testing, homogeneous stresses and strains in the test section at the beginning of the test allow a direct estimation of the material characteristics. At the onset of strain localization, this condition is not valid any more and the test results are usually not considered after this point. Unlike this, the nature of the Nakazima tests is that stresses and strains vary on the tested sample with respect to the position, and are thus not homogeneous. These local strains are therefore not representative for the whole sample. These local strains are significantly higher compared to the tensile response, which is a consequence of a changing (increasing) measurement volume and varying contact conditions during the Nakazima tests. Other effects may also contribute, but the variation in the local strain rate during the Nakazima tests of one order of magnitude (10^{-2} s^{-1}–10^{-1} s^{-1}) as well as in the temperature (typically 10 °C) cannot exclusively explain the deviation between the simulated and experimental results shown in this work.

The calibrated model was employed in the numerical analyses of sheet forming processes. One of the objectives in these numerical analyses was the investigation of parameters affecting the outcome of the Nakazima-type forming test such as friction and material anisotropy. On one hand, it was demonstrated that an increasing friction between the punch and the work-piece offsets the position of localization from the center of the work-piece (not shown here). The added constraint due to the increase in friction was also accommodated by an increase in the force response. On the other hand, the change in the normal anisotropy was shown to result in a shift in the strain path mainly for work-piece geometries having negative minor strain. By way of contrast, the work-piece geometries having positive minor strain accommodate the change in the normal anisotropy only through their force response. For the sake of comparison, an isotropic von Mises yield function was additionally used in the simulations. The respective numerical results clearly showed that the adopted distortional hardening model leads to significantly better predictions.

Fig. 10. Punch force–displacement responses observed in experiments and forming limit simulations obtained for AZ31 assuming a constant *r*-value of 0.12.

r-value is reported. In the case of stress states close to uniaxial tension the *r*-value has a big influence. The previously discussed offset between experimentally and numerically obtained strain paths, see Fig. 6, can thereby be explained. Therefore, in the absence of accurate *r*-value measures at large deformation, the model calibrated based on the constant *r*-value taken at a strain level of 0.12 was now employed for the simulation of the forming limit test for AZ31. The resulting punch force–displacement responses, presented in Fig. 10, generally show a reduced punch force compared to the distortional hardening model, see Fig. 5b. The peak values for geometries I and III are still underestimated. Nevertheless, the forming limits depicted in Fig. 10b are more realistic than the previously obtained ones. For geometries II and V, the strain path exactly follows the experimentally obtained ones, and an assumed imperfection of 1% in the M–K model

Another reason why distortional hardening should be considered is evidenced in Fig. 6b: As already mentioned, the strain path significantly changes in the case of AZ31 for geometry VII. As this happens prior to localization, this effect may be explained by a change of plastic flow direction, resulting from a variation of the yield surface tangent at that position.

The Marciniak and Kuczynski localization criterion, which analyzes plastic instability triggered by geometrical imperfection, was used to predict the forming limits. Apart from the ongoing discussion whether this criterion is suited for positive and negative minor strains, two major influences have been confirmed here. The criterion is sensitive to the underlying plastic potential and the hardening law used. The latter is commonly based on an extrapolation of uniaxial tensile tests beyond the onset of diffuse necking and thus not directly measured. Although the planar anisotropy evidenced by the test has been captured very well by the distortional hardening model used here, the extrapolation of the r-value to strains beyond the localization strain remains arguable. The implicitly assumed increase of the r-value causes an overprediction of the localization. This can successfully be circumvented by fitting the plastic potential to constant r-values, and it remains the choice of the user as to which strain level (and thus r-value) will be considered.

It has been shown by Stutz et al. [34] that microstructure changes occur due to dynamic recrystallization during testing. Thus, differences in the fractions of recrystallized microstructure have been observed for varied strain paths. Qualitatively comparable results have also been presented for uniaxial tensile tests of the same material [35]. However, the onset of recrystallization may be different for tensile tests compared to Nakazima tests, resulting in varying effects on the flow stress of the mechanical tests. As the material model used in this work is triggered by the tensile tests, the flow behavior in the Nakazima tests resulting from dynamic recrystallization is naturally not captured by the model. Hence, it remains a challenge to calibrate model parameters and to use the respective model for predictions – it will, however, be possible once the physical mechanisms in verification simulations and predictions are identical.

Appendix A. A yield function describing magnesium alloys

Considering perfect plasticity (no hardening), the yield function CaBa2004 reads in tensor notation

$$f = \phi(\mathbf{\Sigma}) - \tau_\mathrm{o}^3 \quad \text{with } \phi(\mathbf{\Sigma}) = [J_2^\mathrm{o}(\mathbf{\Sigma})]^{3/2} + J_3^\mathrm{o}(\mathbf{\Sigma}). \tag{A.1}$$

Here and henceforth, τ_o is the (for now constant) yield stress and $J_2^\mathrm{o}(\mathbf{\Sigma})$ and $J_3^\mathrm{o}(\mathbf{\Sigma})$ are the modified second and third invariants of the Mandel stresses $\mathbf{\Sigma}$. They are defined as

$$J_2^\mathrm{o} = \tfrac{1}{2}\,\mathrm{tr}\left(\overline{\mathbf{\Sigma}}_1 \cdot \overline{\mathbf{\Sigma}}_1\right) \quad \text{and} \quad J_3^\mathrm{o} = \tfrac{1}{3}\,\mathrm{tr}\left(\overline{\mathbf{\Sigma}}_2 \cdot \overline{\mathbf{\Sigma}}_2 \cdot \overline{\mathbf{\Sigma}}_2\right), \tag{A.2}$$

where stress tensors $\overline{\mathbf{\Sigma}}_1$ and $\overline{\mathbf{\Sigma}}_1$ follow from the linear transformations

$$\overline{\mathbf{\Sigma}}_1 = \mathbb{H}_1 : \mathbf{\Sigma} \quad \text{and} \quad \overline{\mathbf{\Sigma}}_2 = \mathbb{H}_2 : \mathbf{\Sigma}. \tag{A.3}$$

Here, $\mathbb{H}_i$ are fourth-order tensors. According to Eqs. (A.1)–(A.3) by setting $\mathbb{H}_2 = \mathbf{0}$ and $\mathbb{H}_1 = \mathbb{I} - \frac{1}{3}\mathbf{1} \otimes \mathbf{1}$, a von Mises-type yield function is obtained.

Although the presented constitutive model is conceptually relatively simple, the number of the respective material parameters is very large. To be more precise, with $\tau_\mathrm{o} \in \mathbb{R}$ and $\mathbb{H}_i \in \mathbb{R}^{3\times3\times3\times3}$, 163 material parameters have to be calibrated. That is clearly numerically and physically not practical. However, it turns out that this large number of material parameters can be

significantly reduced by enforcing some physical constraints. These constraints are:

- Major symmetry: Similar to the fourth-order elasticity tensor, $\mathbb{H}_1$ and $\mathbb{H}_2$ are assumed to show major symmetry. That is equivalent to the existence of a potential defining $\mathbb{H}_1$ and $\mathbb{H}_2$ as its Hessian.
- Minor symmetry: Since the Mandel stresses are symmetric (isotropic elastic Neo-Hookean model is used), $\mathbb{H}_1$ and $\mathbb{H}_2$ show minor symmetry, i.e.

$$\mathbb{H}_{klmn} = \mathbb{H}_{lkmn} = \mathbb{H}_{klnm} = \mathbb{H}_{mnkl} \quad \text{for } \mathbb{H}_1 \text{ and } \mathbb{H}_2. \tag{A.4}$$

- Pressure invariance: Since the yield function should be independent with respect to hydrostatic stress states

$$\mathbb{H}_{kkmn} = 0 \quad \text{for } \mathbb{H}_1 \text{ and } \mathbb{H}_2 \tag{A.5}$$

holds.
- Orthotropic material symmetry: Magnesium sheets have an orthotropic mechanical response. In this case, the number of material parameters can be further reduced.

Combining the aforementioned physical constraints, the number of material parameters defining $\mathbb{H}_i$ can be reduced to six. Thus, using Voigt notation (matrix notation) indicated by calligraphic letters ($\mathcal{H}_i$), $\mathbb{H}_i$ can be written as six by six matrices of the type

$$\mathcal{H}_i = \begin{bmatrix} (c_2+c_3)/3 & -c_3/3 & -c_2/3 & 0 & 0 & 0 \\ -c_3/3 & (c_3+c_1)/3 & -c_1/3 & 0 & 0 & 0 \\ -c_2/3 & -c_1/3 & (c_1+c_2)/3 & 0 & 0 & 0 \\ 0 & 0 & 0 & c_4 & 0 & 0 \\ 0 & 0 & 0 & 0 & c_5 & 0 \\ 0 & 0 & 0 & 0 & 0 & c_6 \end{bmatrix}, \quad i=1,2, \tag{A.6}$$

where c_j with $j=1\ldots6$ are the reduced six components of the transformation tensors $\mathcal{H}_1$ and $\mathcal{H}_2$. For plane stress conditions, which is a reasonable assumption in most sheet forming processes, the six components of the transformation tensor can be further reduced to four. As a result, the definition of the yield function (A.1) requires the identification of nine parameters in this case (dim $\mathbb{H}_1$ + dim $\mathbb{H}_2$ + dim $\tau_0 = 9$).

A.1. The evolution of the yield function – hardening models

Suitable hardening models are required to capture the stress–strain responses of the magnesium alloys ZE10 and AZ31. Most frequently, isotropic and kinematic hardening models are applied for that purpose. However, such models do not account for the distortion of the yield function which can also be observed for magnesium. This distortion is due to texture evolution. For incorporating this effect as well, the two transformation tensors $\mathbb{H}_i$ are considered as evolving internal variables. With this assumption, a yield function of the type

$$f = \phi(\mathbf{\Sigma}, \mathbb{H}_1, \mathbb{H}_2) - \tau_\mathrm{o}^3 - [\tau(\alpha)]^3 \tag{A.7}$$

is considered in the present paper. Here, ϕ is defined by Eq. (A.1)$_2$, τ_o is the initial yield stress and τ is a stress-like internal variable associated with isotropic hardening.

The internal variables $\mathbf{Q} = \{\tau; \mathbb{H}_1; \mathbb{H}_2\}$ follow implicitly from the definition of the Helmholtz energy Ψ. Assuming that isotropic and the two distortional hardening mechanisms are uncoupled yields the energy Ψ^pl:

$$\Psi^\mathrm{pl} = \Psi_\mathrm{iso}^\mathrm{pl}(\alpha) + \Psi_\mathrm{dist1}^\mathrm{pl}(\mathbb{E}_1) + \Psi_\mathrm{dist2}^\mathrm{pl}(\mathbb{E}_2) \tag{A.8}$$

with $\mathbb{E}_i$ being dual internal variables conjugate to $\mathbb{H}_i$ and α

denoting the dual to τ. Concerning isotropic hardening, an exponential saturation is assumed. More precisely,

$$\tau(\alpha) = -\partial_\alpha \Psi = \Delta\tau_\infty[1-\exp(\zeta\alpha)] \Rightarrow \Psi_{\text{iso}}^{\text{pl}}$$
$$= \int_{\alpha=0}^{\alpha} \tau\alpha \, d\alpha \qquad (A.9)$$

where α is the strain-like internal variable conjugate to τ, $\Delta\tau_\infty$ and ζ denote two material parameters defining the saturation value and the saturation rate of τ. The isotropic hardening model is completed by considering an associative evolution equation of the type

$$\dot\alpha = \dot\lambda \partial_\tau f. \qquad (A.10)$$

For the sake of simplicity, quadratic functions are assumed to describe distortional hardening. Accordingly,

$$\Psi_{\text{dist}i}^{\text{pl}}(\mathbb{E}_i) = \tfrac{1}{2}H_i\mathbb{E}_i :: \mathbb{E}_i \qquad (A.11)$$

where H_i denotes the hardening modulus. In line with isotropic hardening, evolution equations for the internal variables $\mathbb{H}_i$ or $\mathbb{E}_i$ are required. However, due to the tensorial nature of $\mathbb{H}_i$ and $\mathbb{E}_i$ the development of such evolution equations is not straightforward, since they have to fulfill certain physical principles. While the proposed framework automatically fulfills the principle of material frame indifference, that is not the case for the second law of thermodynamics. In order to derive a physically sound model which also fulfills the second law of thermodynamics, the reduced dissipation inequality is considered. After a straightforward calculation it reads

$$\mathcal{D} = \boldsymbol{\Sigma} : \boldsymbol{L}^{\text{pl}} + \tau\dot\alpha + \mathbb{H}_1 :: \dot{\mathbb{E}}_1 + \mathbb{H}_2 :: \dot{\mathbb{E}}_2 \geq 0. \qquad (A.12)$$

Here, the elastic response $\boldsymbol{\Sigma} = 2\mathbf{Ce} \cdot \partial_{\mathbf{Ce}}\Psi$ has already been inserted. Since the function $\phi-\tau^3$ is positively homogeneous of degree three with respect to $(\boldsymbol{\Sigma},\tau)$, Eq. (A.12) can be rewritten as

$$\mathcal{D} = 3\dot\lambda\tau_0^3 + \mathbb{H}_1 :: \dot{\mathbb{E}}_1 + \mathbb{H}_2 :: \dot{\mathbb{E}}_2 \geq 0. \qquad (A.13)$$

The first term is evidently greater than zero. A sufficient condition for guaranteeing the dissipation inequality is consequently given by

$$\mathcal{D}_{\text{dist}i} := \mathbb{H}_i :: \dot{\mathbb{E}}_i \geq 0. \qquad (A.14)$$

Now assuming that distortional hardening is only driven by the internal variable, Eq. (A.14) simplifies to

$$\mathcal{D}_{\text{dist}i} = \mathbb{H}_i :: \frac{\partial\mathbb{E}_i}{\partial\alpha}\dot\alpha \geq 0. \qquad (A.15)$$

The viscoplastic rate effect observed within the experiments is captured by replacing the rate-independent isotropic hardening variable τ (see Eq. (A.7)) in the yield function by its rate-dependent counterpart

$$\tau_{\text{rate}} = \tau\left(\frac{\dot\alpha}{\beta}\right)^n. \qquad (A.16)$$

Here, β and n are model parameters. According to this choice, a rate effect is only accounted for the isotropic hardening part. The shape of the yield function (distortional hardening) is thus rate-independent.

The assumption $\mathbb{E}_i = \mathbb{E}_i(\alpha)$ is a good approximation for radial loading paths and thus complies with the experimental setup. Since $\mathbb{H}_i = -H_i\mathbb{E}_i$, $\mathbb{H}_i = \mathbb{H}_i(\alpha)$ represents an equivalent assumption. Within the material parameter calibration exponential functions

$$c_j(\alpha) = A_j + B_j(1-\exp(-C_j\alpha)) \qquad (A.17)$$

were adopted where A_j, B_j and C_j with $j=\{1\ldots6\}$ are the model parameters (for each $\mathbb{H}_i$). In line with Eq. (A.6), the coefficients c_j in Eq. (A.17) denote the components defining the tensors $\mathbb{H}_i$.

References

[1] D. Banabic, H.J. Bunge, K. Poehlandt, A.E. Tekkaya, Formability of Metallic Materials, Springer, 2000.
[2] A. Barata da Rocha, A.D. Santos, P. Teixeira, M.C. Butuc, J. Mater. Process. Technol. 209 (11) (2009) 5097–5109.
[3] F. Barlat, D. Lege, J. Brem, Int. J. Plast. 7 (7) (1991) 693–712.
[4] J. Bohlen, M. Nuernberg, J. Senn, D. Letzig, S. Agnew, Acta Mater. 55 (2007) 2101–2112.
[5] H.J. Bong, F. Barlat, M.G. Lee, D.C. Ahn, Int. J. Mech. Sci. 64 (1) (2012) 1–10.
[6] M. Butuc, Forming Limit Diagrams. Definition of Plastic Instability Criteria, Ph.D. Thesis, Engineering Faculty of Porto University, March 2004.
[7] O. Cazacu, F. Barlat, J. Math. Mech. Solids 6 (2001) 513–630.
[8] O. Cazacu, F. Barlat, Int. J. Plast. 20 (2004) 2027–2045.
[9] C.L. Chow, L.G. Yu, W.H. Tai, M.Y. Demeri, Int. J. Mech. Sci. 43 (2) (2001) 471–486.
[10] E. Doege, T. El-Dsoki, D. Seibert, J. Mater. Process. Technol. 50 (1–4) (1995) 197–206.
[11] D. Drucker, J. Appl. Mech. (1949) 349–357.
[12] S. Ertürk, W. Brocks, J. Bohlen, D. Letzig, D. Steglich, Int. J. Mater. Form. 5 (4) (2011) 325–339.
[13] G.M. Goodwin, Application of Strain Analysis to Sheet Metal Forming Problems in the Press Shop, Technical Report, Society of Automotive Engineers, 1968.
[14] V. Hasek, On the Strain and Stress States in Drawing of Large Irregular Sheet Metal Components, Technical Report, University of Stuttgart, 1973.
[15] V.V. Hasek, Blech Rohre Profile 25 (1978) 213–220.
[16] V.V. Hasek, Blech Rohre Profile 25 (1978) 285–292.
[17] V.V. Hasek, Blech Rohre Profile 25 (1978) 493–499.
[18] R. Hill, Proc. R. Soc. A 193 (1948) 281–297.
[19] R. Hill, J. Mech. Phys. Solids 1 (1952) 19–30.
[20] R. Hill, J. Mech. Phys. Solids 38 (1990) 405–417.
[21] J. Hutchinson, K. Neale, Mech. Sheet Metal Form. (1978) 111–126.
[22] J. Hutchinson, K. Neale, Mech. Sheet Metal Form. (1978) 127–153.
[23] J. Hutchinson, K. Neale, Mech. Sheet Metal Form. (1978) 269–285.
[24] A. Karafillis, M. Boyce, J. Mech. Phys. Solids 41 (1993) 1859–1886.
[25] S. Keeler, W. Backofen, Trans. ASM 56 (1963) 25–48.
[26] S.P. Keeler, Determination of Forming Limits in Automotive Stampings, Technical Report, Society of Automotive Engineers, 1965.
[27] M. Kuroda, V. Tvergaard, J. Solids Struct. 37 (2000) 5037–5059.
[28] Z. Marciniak, K. Kuczynski, Int. J. Mech. Sci. 9 (1967) 609–620.
[29] Z. Marciniak, K. Kuczynski, T. Pokora, Int. J. Mech. Sci. 15 (1973) 789–805.
[30] M.N. Mekonen, D. Steglich, J. Bohlen, D. Letzig, J. Mosler, Mater. Sci. Eng. A 540 (2012) 174–186.
[31] K. Nakazima, T. Kikuma, K. Hasuka, Study on the Formability of Steel Sheets, Technical Report, Yawata, 1971.
[32] J.W. Signorelli, M.A. Bertinetti, P.A. Turner, Int. J. Plast. 25 (1) (2009) 1–25.
[33] D. Steglich, W. Brocks, J. Bohlen, F. Barlat, Int. J. Mater. Form. 4 (2) (2011) 243–253.
[34] L. Stutz, J. Bohlen, D. Letzig, K.-U. Kainer, Formability of magnesium sheet ZE10 and AZ31 with respect to initial texture, in: Magnesium Technology, 2011, pp. 373–378.
[35] L. Stutz, J. Bohlen, D. Letzig, K.-U. Kainer, Effect of strain rate and temperature on the tensile properties of magnesium sheets AZ31 and ZE10 at elevated temperatures, in: Mg2012: 9th International Conference on Magnesium Alloys and their Applications, Wiley, 2012, pp. 593–598.
[36] H. Swift, J. Mech. Phys. Solids 1 (1952) 1–16.
[37] S. Yi, J. Bohlen, F. Heinemann, D. Letzig, Acta Mater. 58 (2010) 592–605.